Supplement of

Tracking surface ozone responses to clean air interventions under a warming climate in China

This supporting information contains the follows:

Number of pages: 27

Number of methods: S1-S3

Number of tables: S1-S8

Number of figures: S1-S18

Supporting Methods

S1. Uncertainty analysis for FEA method

To assess the uncertainty associated with the FEA method, we applied a cross-matrix validation approach, training models for each year as the baseline year (i.e., using each year as a reference for emissions) to calculate the relative contribution of anthropogenic emissions in different years. Specifically, we alternated the role of each year as the model training year (i.e., the fixed emission reference year) and the prediction year. As illustrated in Eqs. S1 and S2, for any two years, n and m, they can both serve as either the model training year or the model prediction year. For instance, $\Delta ANT_{n(m)}$ represents the scenario where year n is used as the model training year and year m as the model prediction year, while $\Delta ANT_{m(n)}$ denotes the reverse, with year m as the model training year and year n as the model prediction year.

$$\Delta ANT_{n(m)} = OBS_m - Pred_{n(m)} - RES_n \quad \text{(S1)}$$

$$\Delta ANT_{m(n)} = OBS_n - Pred_{m(n)} - RES_m \quad \text{(S2)}$$

From Eq. (S1), the observed data for year m (OBS_m) can be expressed as the sum of $Pred_{n(m)}$, RES_n, and $\Delta ANT_{n(m)}$. Theoretically, if there were no uncertainty in the use of data from different years for model training, then $\Delta ANT_{n(m)} = -\Delta ANT_{m(n)}$. Therefore, the uncertainty $u_{n(m)}$ associated with the FEA method can be represented by Eq. S3:

$$u_{n(m)} = \frac{(Pred_{n(m)} + RE_n - (OBS_n - Pred_{m(n)} - RE_m)) - OB_m}{OBS_m} \quad \text{(S3)}$$

S2. COVID-19 Lockdown Driven Computation Based on FEA Method

Wuhan, where the outbreak of the virus was first detected, issued a lockdown policy on January 23, 2020, followed by outbreaks in other Chinese cities within the next few days. A strict national quarantine lasting one to two months was then imposed. Most Chinese cities gradually relaxed their quarantine measures starting in April, and Wuhan reopened on April 8th. Therefore, we consider the first four months of 2020 as the COVID-19 Lockdown period (LD) by referring to the definition of COVID-19 lockdown by Geng et al. (2024). The difference between the observed MDA8 ozone concentration in LD (Obs_{LD}) and the corresponding model prediction ($Pred_{(i,LD)}$) is scaled by the ratio of the samples in LD (n_{LD}) to the total number of samples in 2020 (n_{All}) (i.e., $C_{LD} = n_{LD}/n_{All}$). This value represents the combined contribution of short-term unconventional emission reductions and long-term conventional emission control policies during the COVID-19 lockdown. The impact of long-term conventional emission reductions is estimated by the difference between observed and predicted MDA8 ozone concentrations during non-blockade periods ($Obs_{NLD} - Pred_{(i,NLD)}$), scaled by C_{LD}. Thus, the relative contribution of COVID-19 lockdown to the MDA8 ozone trend（$COVID_{(i,LD)}$）can be calculated by Eq. S4:

$$COVID_{(i,LD)} = C_{LD} \times \left(OBS_{LD} - P_{(i,LD)}\right) - C_{LD} \times \left(OBS_{NLD} - P_{(i,NLD)}\right) \quad \text{(S4)}$$

S3. Quantification of extreme weather-driven changes in ozone

An unprecedented and prolonged heat wave in the summer of 2022 struck central and eastern China, with the most severely affected area being the Yangtze River basin (Wang et al., 2023; Zhang et al., 2023), identified as the longest-lasting and most intense heat wave since at least 1961 (Mallapaty, 2022). The Yangtze-Huaihe region, where the prolonged rainfall occurs, is also a region of frequent sustained extreme precipitation events (Yin et al., 2020). The opening of the "rainy season" is marked in late June with the northward push of the East Asian summer winds and the first northward jump of the subtropical high-pressure ridgeline in the western Pacific Ocean, and generally lasts until mid-July.

We employed the SHapley Additive exPlanations (SHAP) method (Lundberg et al., 2020) to elucidate the potential impacts of all input features k on the predictions of the RF model. SHAP assigns an importance score to each feature, revealing their respective contributions to model predictions. Positive values indicate a beneficial influence on predictions, while negative values denote adverse effects. The extreme heatwave events in 2022 (HW) and prolonged rainfall (PR) provide unique and realistic atmospheric environments for us to explore the effects of typical weather extremes on ozone. The PR period is defined as June 15 to July 15 each year, with the remaining period from June to August categorized as the non-plum rain period (NPR). To isolate the effects of the rainy season, we defined the HW event in 2022 as occurring from July 16 to August 31, while the corresponding periods in other years were considered non-heatwave (NHW) periods. We first calculated the SHAP values for input features during PR and NPR, as well as HW and NHW periods. The relative changes in SHAP values ($\Delta SHAP$) between these conditions were used to assess the responses of MDA8 ozone to the rainy season and the 2022 heatwave, as per the following Eqs:

$$\Delta SHAP_k = SHAP_{PR} - SHAP_{NPR} \quad \text{(S6)}$$

$$\Delta SHAP_k = SHAP_{HW} - SHAP_{NHW} \quad \text{(S7)}$$

Supporting Tables

Table S1. Overview of the characteristics of the ERA5 variables used in the analysis of this study.

Abbreviations	Description
T2m	Temperature at 2m (K)
SR	Short wave solar radiation (W/m^2)
SP	Sea level pressure (Pa)
BLH	Boundary layer height (m)
TP	Total precipitation (m)
RH	Surface relative humidity (%)
TCC	Total cloud cover
U10	Zonal wind at 10m ($m\ s^{-1}$)
V10	Meridional wind at 10m ($m\ s^{-1}$)
U850	Zonal wind at 850 hPa ($m\ s^{-1}$)
V850	Meridional wind at 850 hPa ($m\ s^{-1}$)
W850	Vertical velocity at 850 hPa ($Pa\ s^{-1}$)
U650	Zonal wind at 650 hPa ($m\ s^{-1}$)
V650	Meridional wind at 650 hPa ($m\ s^{-1}$)
W650	Vertical velocity at 650 hPa ($Pa\ s^{-1}$)
U500	Zonal wind at 500 hPa ($m\ s^{-1}$)
V500	Meridional wind at 500 hPa ($m\ s^{-1}$)
W500	Vertical velocity at 500 hPa ($Pa\ s^{-1}$)
LAI(hv)	Leaf area index, high vegetation ($m^2\ m^{-2}$)
LAI(lv)	Leaf area index, low vegetation ($m^2\ m^{-2}$)

Table S2. Definitions of the 7 statistical indicators used in this study.

No.	Statistics (abbreviation)	Definition	Note
1.	Mean Absolute Error (MAE)	$MAE = \frac{1}{n}\sum_{i=1}^{n}\lvert P_i - O_i\rvert$	μg m^{-3}
2.	Root mean square error(RMSE)	$RMSE = \sqrt{\frac{\sum_{i=1}^{n}(P_i - O_i)^2}{n}}$	μg m^{-3}
3.	Normalized Mean Squared Error(NMSE)	$NMSE = \frac{1}{n}\sum_{i=1}^{n}\frac{MSE}{VAR(P_i)}$	Unitless, 0 ≤ NMSE ≤ 1
4.	Correlation coeffcient(R)	$R = \frac{\sum_{i=1}^{n}(O_i - \bar{O})(P_i - \bar{P})}{\sqrt{\sum_{i=1}^{n}(P_i - \bar{P})^2 \sum_{i=1}^{n}(O_i - \bar{O})^2}}$	Unitless, -1 ≤ R ≤ 1
5.	Mean bias (MB)	$MB = \frac{1}{n}\sum_{i=1}^{n}(P_i - O_i)$	μg m^{-3}
6.	Normalized mean bias(NMB)	$NMB = \frac{\sum_{i=1}^{n}(P_i - O_i)}{\sum_{i=1}^{n} O_i} \times 100$	-100% ≤ NMB ≤ +∞
7.	Index of Agreement (IOA)	$IOA = 1 - \frac{\sum_{i=1}^{n}(P_i - O_i)^2}{\sum_{i=1}^{n}(\lvert P_i - \bar{O}\rvert + \lvert O_i - \bar{O}\rvert)^2}$	Unitless, 0 ≤ IOA ≤ 1

Table S3. Ten -fold cross-validation results of RF models for national input datasets.

O_3	MAE	RMSE	NMSE	R	MB	NMB	IOA
2015	13.8	20.9	0.06	0.88	0.07	21	0.93
2016	13.7	20.4	0.06	0.89	0.05	20	0.94
2017	14.3	21.3	0.05	0.90	0.06	19	0.95
2018	14.8	21.8	0.05	0.90	0.06	16	0.94
2019	14.1	20.7	0.05	0.90	0.02	17	0.94
2020	12.9	19.1	0.05	0.90	0.03	16	0.94
2021	13.2	19.2	0.05	0.90	0.01	15	0.94
2022	12.7	18.8	0.04	0.91	-0.004	13	0.95
2023	13.0	18.8	0.04	0.91	-0.02	12	0.95

Table S4. Ten-fold cross-validation results of RF models for BTH input datasets.

O_3	MAE	RMSE	NMSE	R	MB	NMB	IOA
2015	14.9	19.9	0.04	0.93	0.01	17	0.96
2016	15.0	20.2	0.04	0.94	0.09	21	0.96
2017	16.2	21.5	0.03	0.94	0.02	17	0.97
2018	16.7	21.9	0.03	0.94	0.09	12	0.96
2019	15.3	20.2	0.03	0.94	-0.04	12	0.97
2020	13.6	18.0	0.02	0.94	-0.06	10	0.96
2021	14.0	18.4	0.03	0.94	-0.02	11	0.96
2022	12.6	16.9	0.02	0.95	-0.06	8	0.97
2023	12.7	16.9	0.02	0.95	-0.12	6	0.97

Table S5. Ten -fold cross-validation results of RF models for FWP input datasets.

O_3	MAE	RMSE	NMSE	R	MB	NMB	IOA
2015	11.6	15.7	0.03	0.94	0.04	13	0.96
2016	12.9	17.5	0.03	0.93	0.05	14	0.96
2017	14.8	19.8	0.03	0.95	0.07	14	0.97
2018	15.0	19.9	0.03	0.94	0.06	14	0.96
2019	13.8	18.2	0.03	0.95	0.12	15	0.97
2020	13.0	17.4	0.03	0.94	-0.02	17	0.97
2021	14.1	18.8	0.03	0.94	0.04	14	0.96
2022	12.6	16.9	0.02	0.95	-0.1	13	0.97
2023	12.4	16.6	0.02	0.95	0.02	10	0.97

Table S6. Ten -fold cross-validation results of RF models for YRD input datasets.

O_3	MAE	RMSE	NMSE	R	MB	NMB	IOA
2015	17.2	26.6	0.09	0.85	0.11	27	0.91
2016	16.6	24.2	0.07	0.87	0.07	20	0.93
2017	17.0	24.5	0.06	0.89	0.06	20	0.94
2018	16.7	23.9	0.06	0.9	0.08	16	0.94
2019	16.3	22.7	0.05	0.9	0.09	18	0.94
2020	15.6	22.4	0.07	0.87	0.12	21	0.92
2021	14.9	21.5	0.06	0.9	0.02	16	0.94
2022	16.1	22.2	0.05	0.89	0.12	13	0.94
2023	15.7	21.8	0.05	0.9	-0.04	15	0.94

Table S7. Ten -fold cross-validation results of RF models for SCB input datasets.

O_3	MAE	RMSE	NMSE	R	MB	NMB	IOA
2015	21.8	31.2	0.14	0.72	0.06	39	0.83
2016	23.3	33.0	0.15	0.72	0.08	44	0.83
2017	24.3	34.1	0.15	0.72	0.04	48	0.83
2018	24.2	34.3	0.14	0.71	0.03	34	0.82
2019	23.4	33.2	0.15	0.72	0.05	37	0.83
2020	20.9	29.3	0.13	0.73	0.04	31	0.83
2021	20.7	29.0	0.11	0.75	0.07	26	0.85
2022	21.0	29.6	0.09	0.77	0.02	24	0.86
2023	20.8	29.3	0.10	0.75	0.01	21	0.85

Table S8. Ten -fold cross-validation results of RF models for PRD input datasets.

O_3	MAE	RMSE	NMSE	R	MB	NMB	IOA
2015	9.3	14.5	0.05	0.94	0.11	17	0.96
2016	11.5	18.0	0.06	0.93	0.11	20	0.95
2017	9.6	16.1	0.07	0.93	0.06	21	0.96
2018	12.2	18.4	0.06	0.92	0.11	23	0.95
2019	10.8	16.3	0.06	0.93	0.07	21	0.95
2020	7.7	12.3	0.04	0.95	-0.03	14	0.97
2021	9.8	14.8	0.05	0.93	-0.004	14	0.96
2022	8.7	13.5	0.04	0.94	0.09	13	0.96
2023	9.5	14.0	0.05	0.93	0.05	14	0.96

Supporting Figures

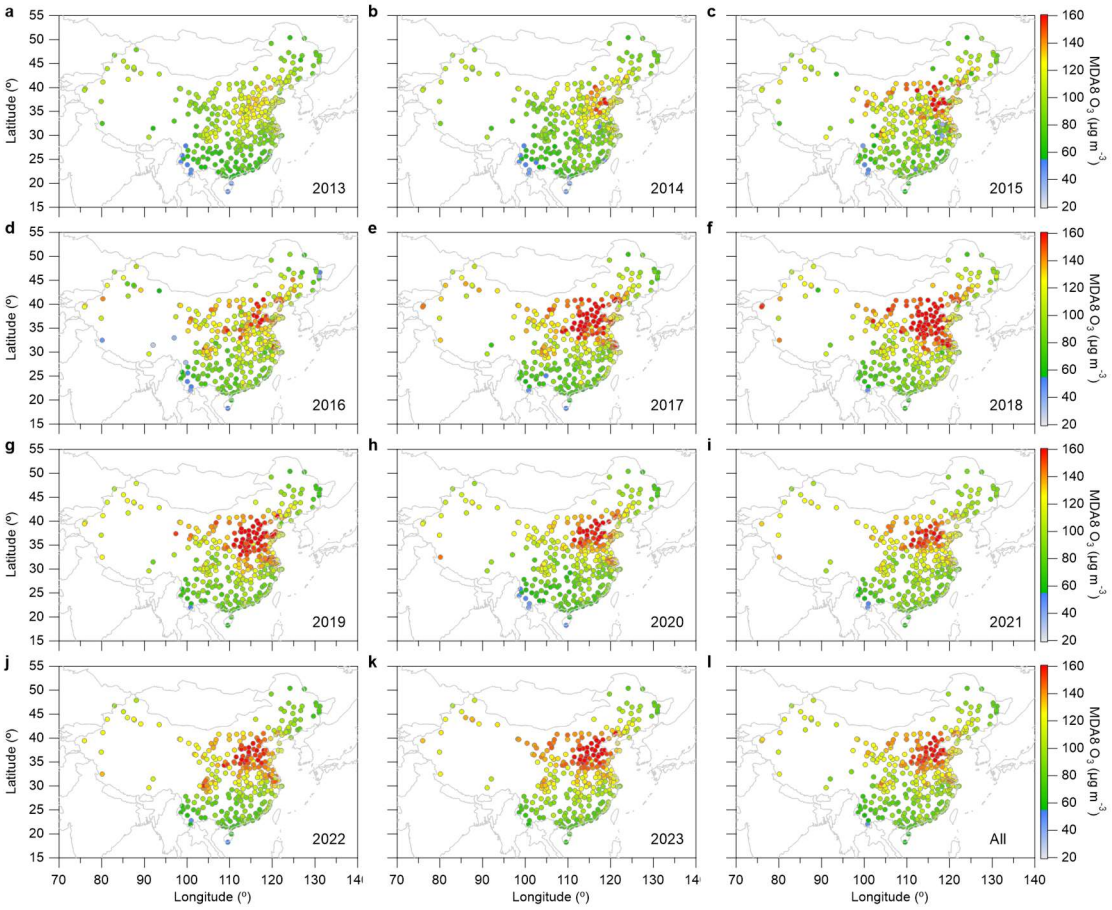

Figure S1. Spatial distribution of MDA8 ozone from 2013 to 2023. This figure displays the mass concentrations of MDA8 ozone in 354 cities across China during the summer months (June-July-August) from 2013 to 2023. The final sub-panel (l) illustrates the average MDA8 ozone concentration over the 11-year period.

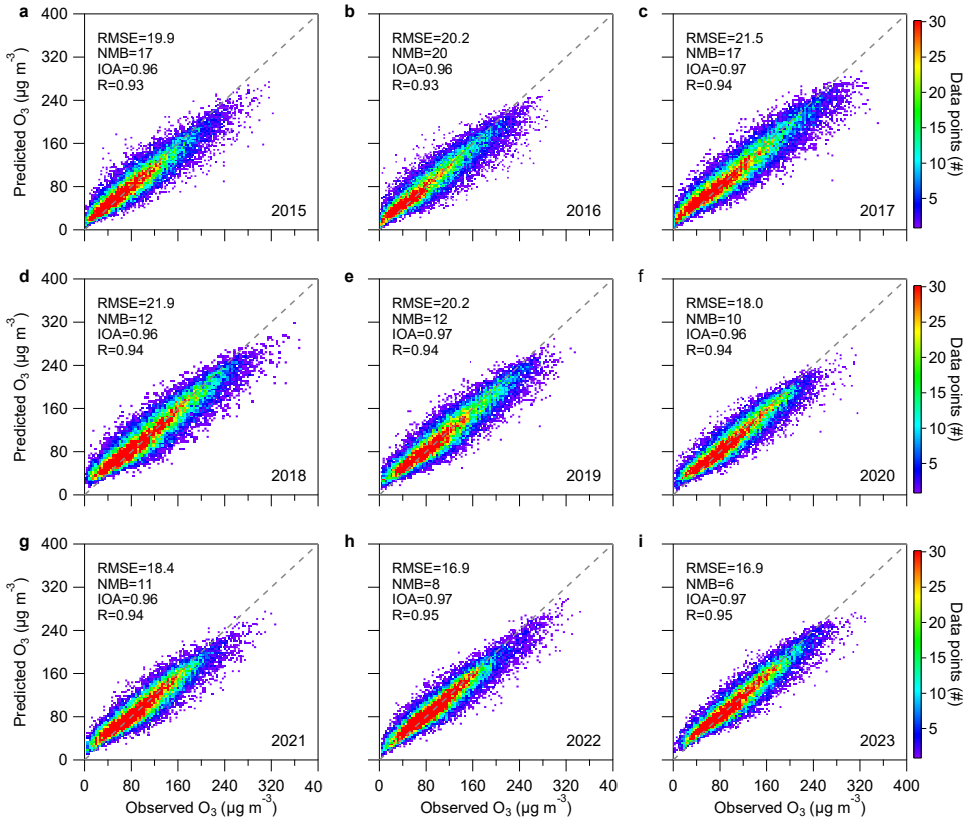

Figure S2. Model performance evaluation. Results of ten-fold cross-validation comparing observed and predicted values for the test set of the RF models for each year from 2015 to 2023 in the BTH region, using this region as an example.

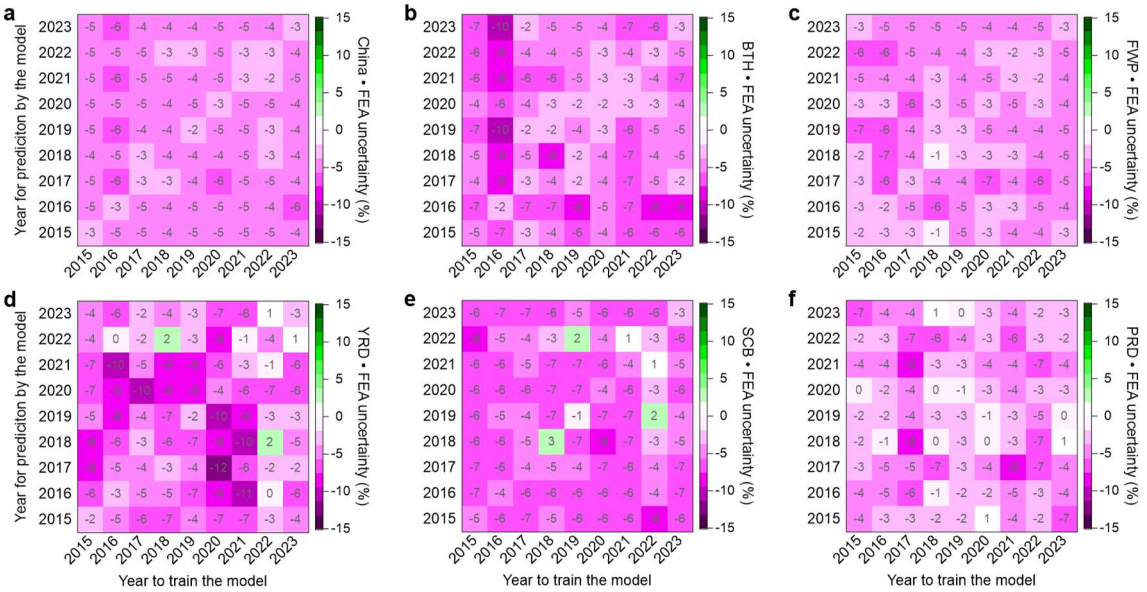

104

105 **Figure S3. Uncertainty of the FEA method.** The uncertainty for the FEA method is calculated using
106 the approach described in Supporting Method S1. The diagonal line in each sub-panel represents the
107 changes in the residuals of the models.

108

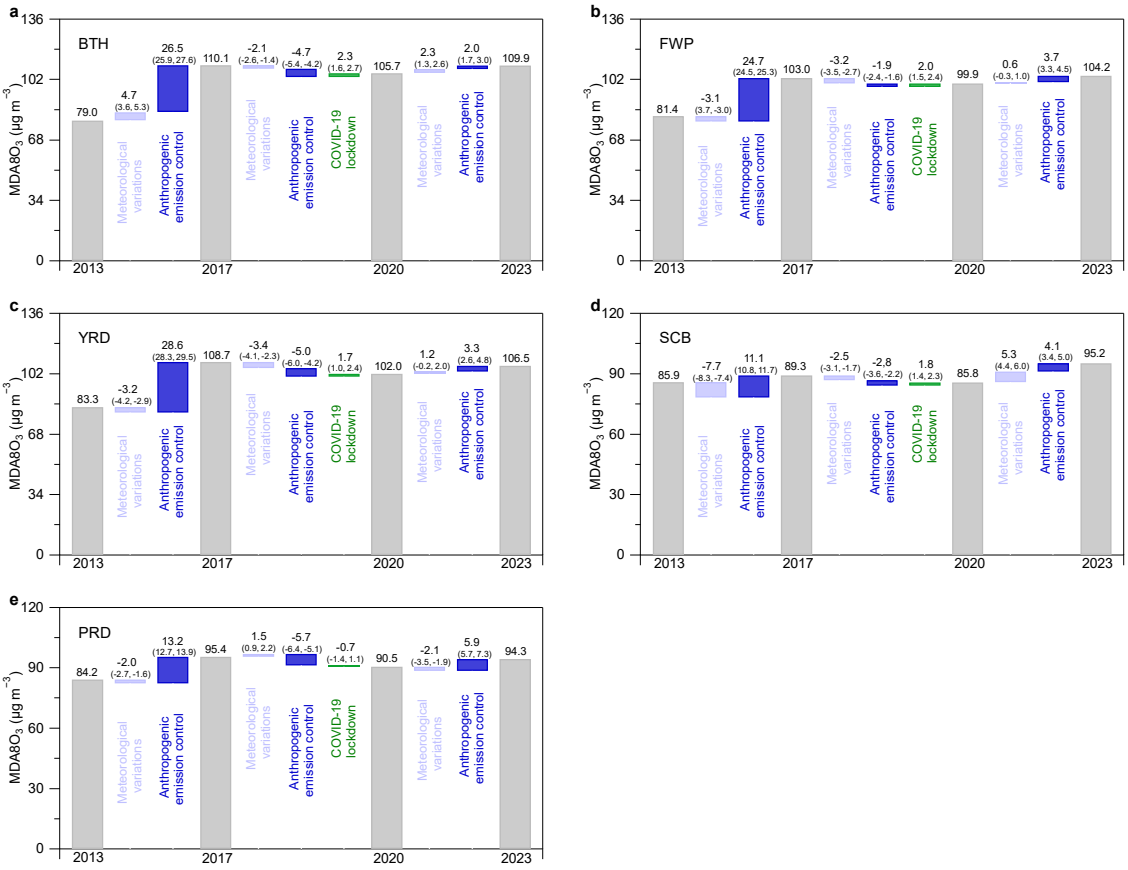

Figure S4. Driving factors of MDA8 ozone from 2013 to 2023. The panels show the contributions of meteorological changes, human emission controls, and the COVID-19 lockdown to the interannual variations of MDA8 ozone in five key regions of China. The values in parentheses represent the 25th to 75th percentile range derived from the FEA method.

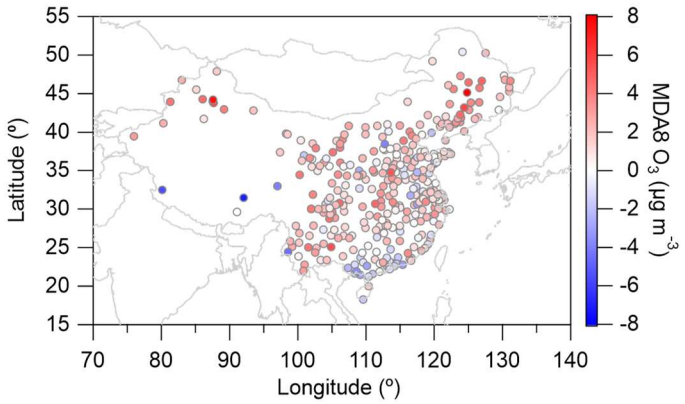

115

116 **Figure S5. Distribution of the relative contribution of the COVID-19 lockdown to MDA8 ozone in**
117 **Chinese cities.** The quantified results in the figure were derived using the formula in Supporting Method
118 S2.

119

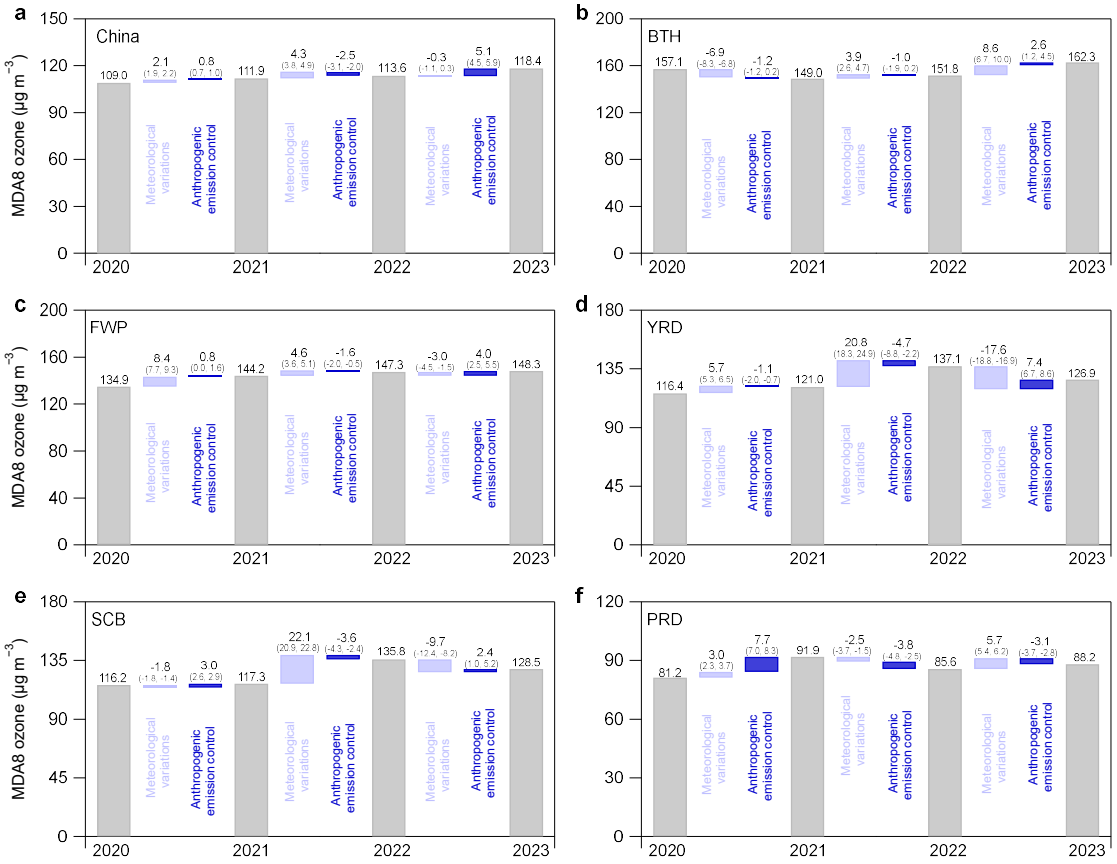

Figure S6. Anthropogenic and meteorological drivers of ozone trends from 2020 to 2023. Changes in summer MDA8 ozone concentrations were decomposed into contributions from anthropogenic emissions and meteorological variability using the FEA framework. Results reflect ensemble estimates based on multiple baseline years (2015–2023) for emissions. Boxplots indicate the interquartile range, with values in parentheses denoting the 25th and 75th percentiles across all baseline scenarios.

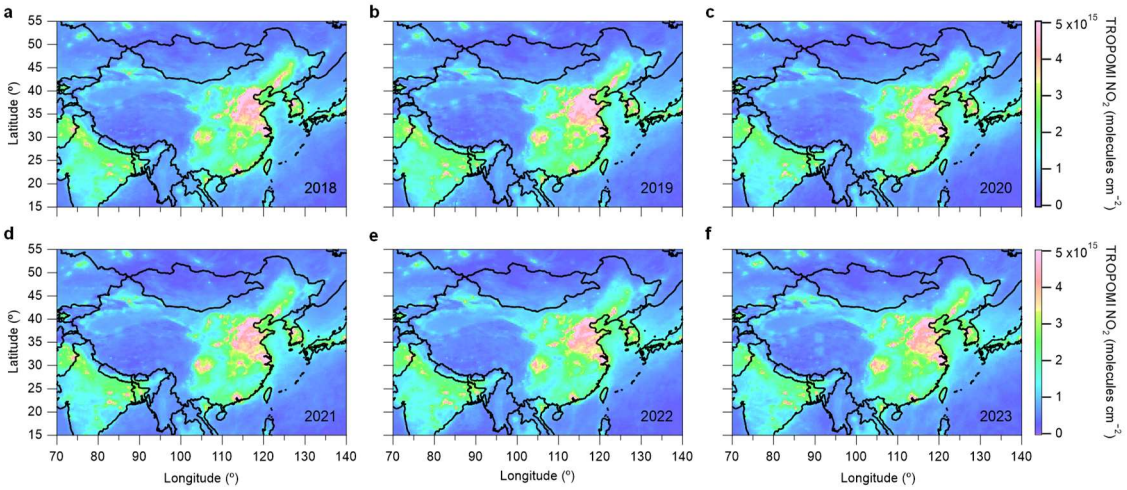

Figure S7. Spatial and temporal variations of satellite NO_2. Map of average levels of satellite-observed NO_2 from June-August 2018 to 2023**.**

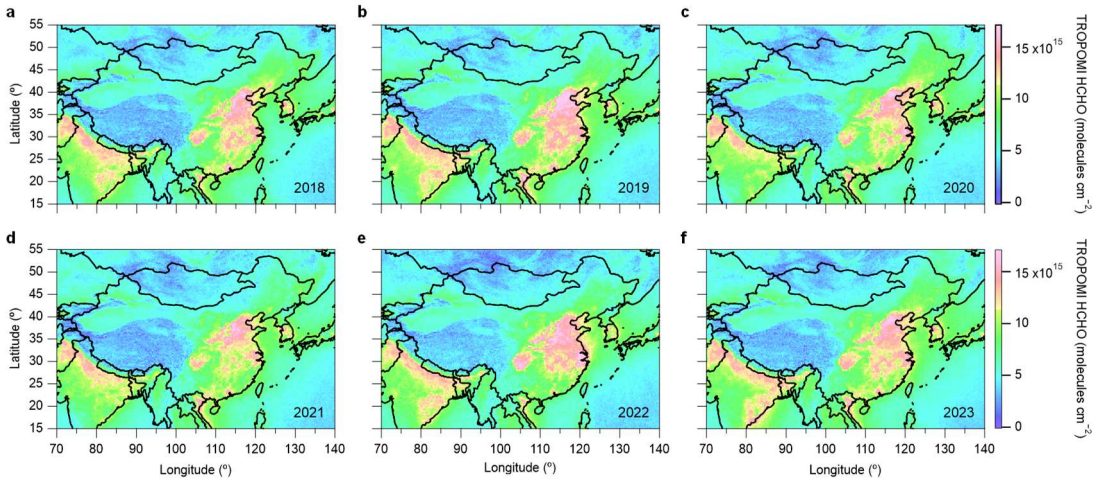

Figure S8. Spatial and temporal variations of Satellite HCHO. Map of average levels of satellite-observed HCHO from June-August 2018 to 2023.

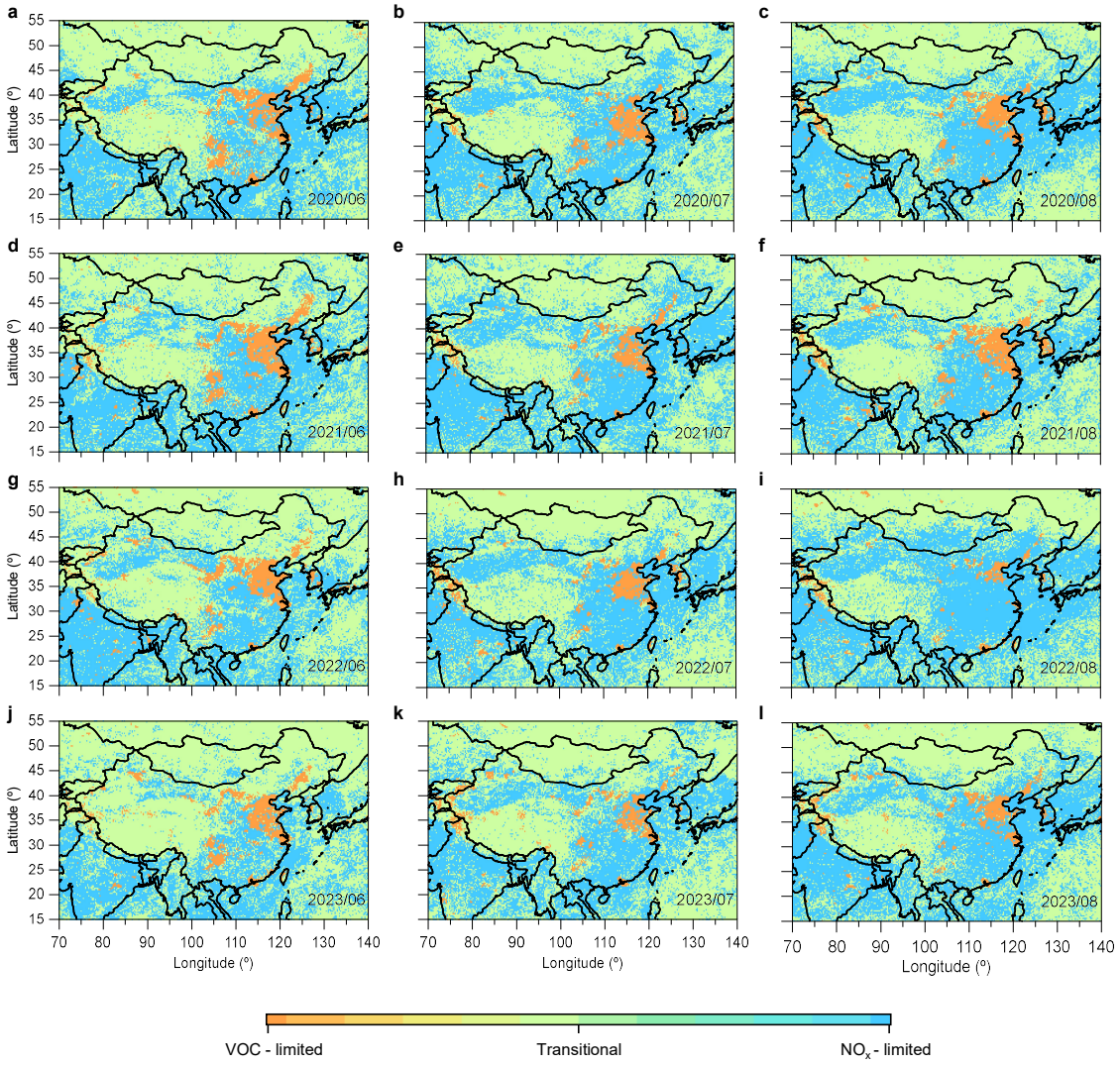

135

136 **Figure S9. Ozone formation sensitivity regimes.** The month-by-month results of FNR analysis from
137 June to August (2018-2023) month-by-month are presented, showing the spatiotemporal variation of
138 ozone sensitivity in different regions. The colors in the map represent the geographical distribution of
139 VOC-limited, NO_x-limited, and transitional ozone sensitivity zones.

140

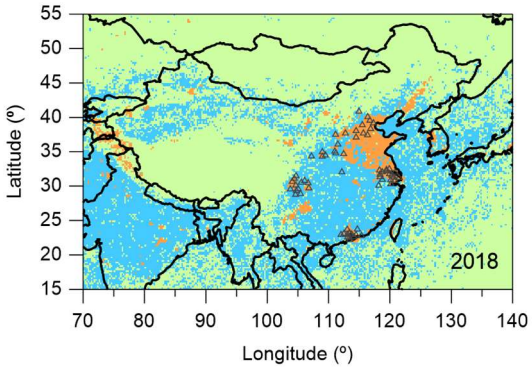

Figure S10. Distribution of urban agglomerations. The panel shows the ozone formation mechanism in China in 2018, with gray triangles representing the longitude and latitude of urban locations in five key regions (BTH, FWP, YRD, SCB, PRD).

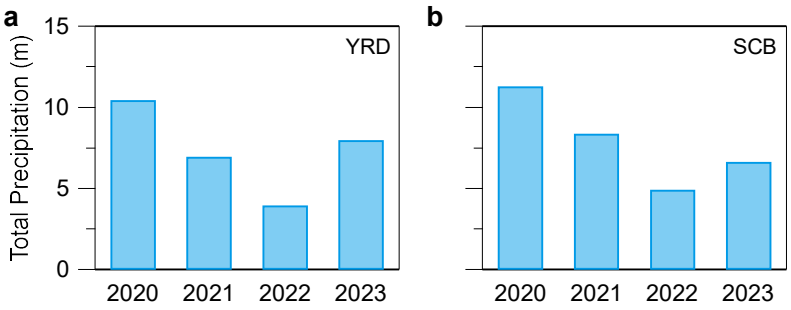

146

147 **Figure S11. Interannual variation in total precipitation.** Total precipitation in the SCB and YRD
148 regions from June to August 2020 to 2023.

149

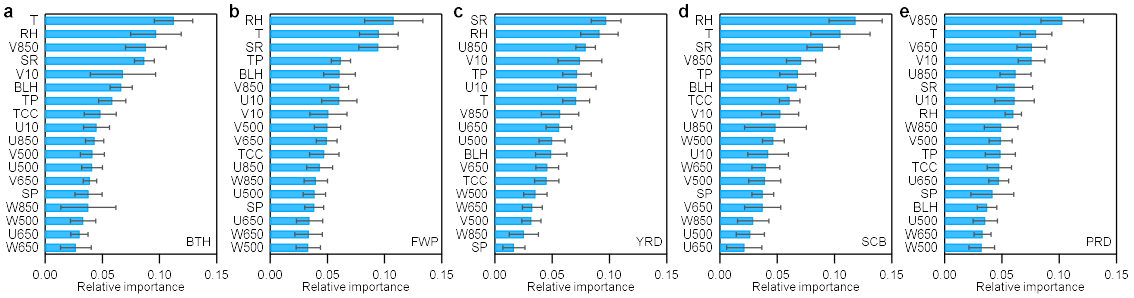

150

151 **Figure S12. Predicting the relative importance of characteristics.** The RF model has built-in

152 importance (mean reduced impurity) for each predicted feature in each of the five typical regions.

153

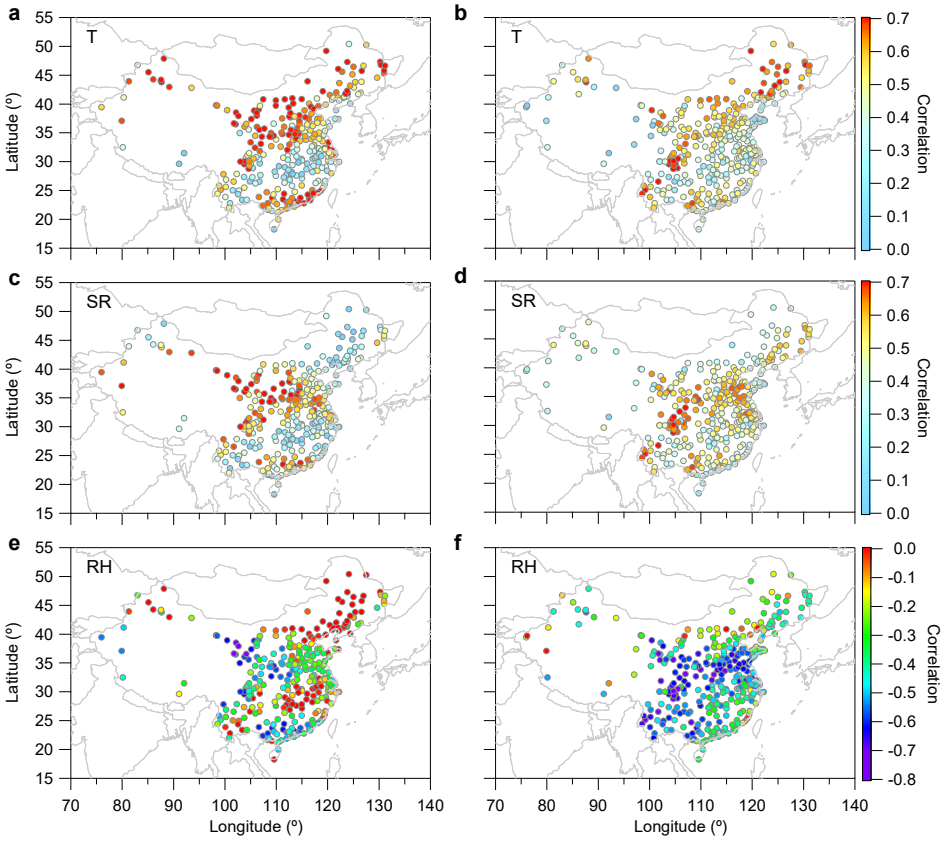

154

155 **Figure S13. Comparison of MDA8 ozone correlations with meteorological conditions during HW**
156 **(left) and NHW (right).** Spatial distribution of MDA8 ozone correlation with T(a), SR(c), RH (e) for
157 354 cities in China from from 15th July to 31st August in 2022, and spatial distribution of MDA8 ozone
158 correlation with T(b), SR(d), RH(f) for 354 cities in China from from 15th July to 31st August during
159 2015-2021 and in 2023.

160

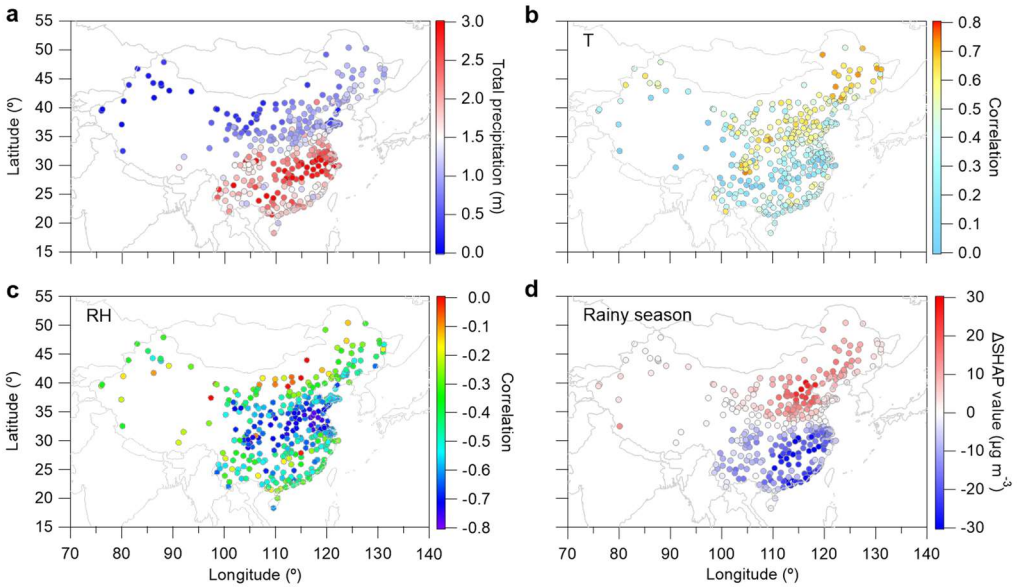

Figure S14. Impact of the prolonged rainfall season on MDA8 ozone. Total rainfall (a), correlation of MDA8 ozone with temperature (c) and relative humidity (d), and total relative contribution of meteorological conditions to MDA8 ozone (d) for 354 cities in China during the rainy season (from 15th June to 15th July) in the PR season during 2015-2023.

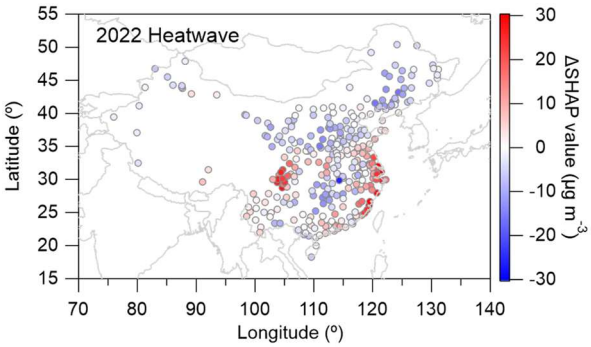

Figure S15. Impact of the 2022 heatwave on MDA8 ozone. Total relative contribution of meteorological conditions to MDA8 ozone during the 2022 heatwave wave (from 15th July to 31st August).

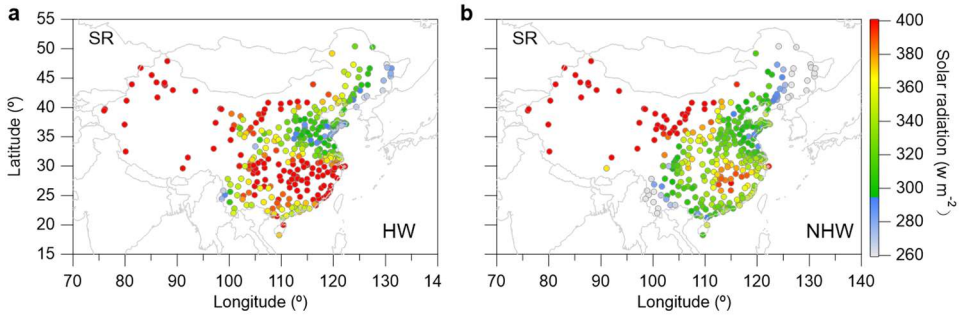

172

173 **Figure S16. Comparison of solar radiation between the HW and NHW periods.** Temporal and spatial
174 distribution of daytime (10:00-17:00) mean solar radiation during the HW and NHW periods.

175

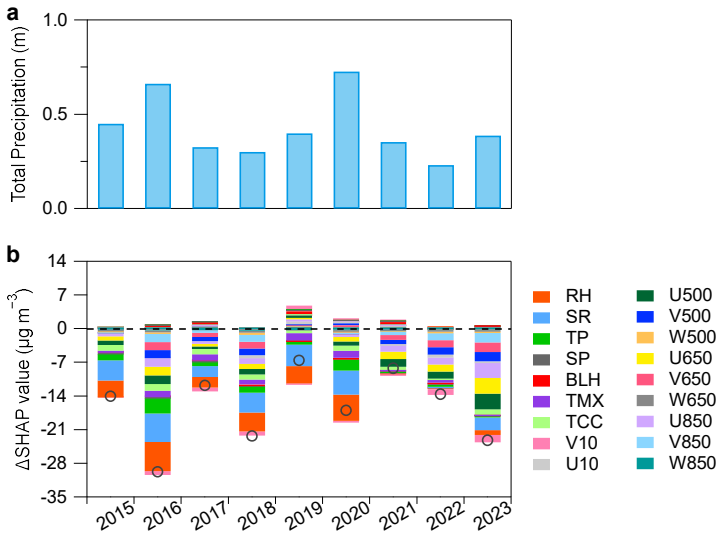

Figure S17. Impact of the rainy season on ozone concentrations. a. Interannual variations in mean daily precipitation in the Yangtze-Huaihe region during the PR period. **b.** Relative contributions of meteorological conditions to MDA8 ozone from 2015 to 2023.

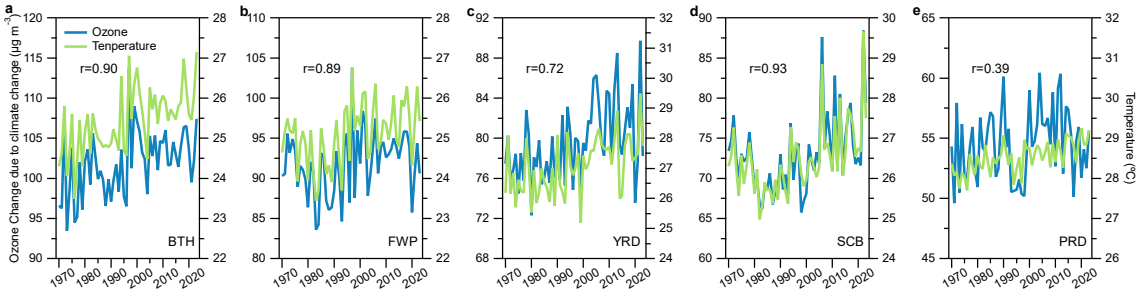

Figure S18. Correlation between summer ozone and mean surface temperature. changes in mean surface temperature and changes in mean ozone concentration driven by climate change over the period 1970 to 2023 (June-August). Correlation coefficients (r) between ozone and mean surface temperature for different regions are given in each panel.

References

Geng, G., Liu, Y., Liu, Y., Liu, S., Cheng, J., Yan, L., Wu, N., Hu, H., Tong, D., Zheng, B., Yin, Z., He, K., Zhang, Q.: Efficacy of China's clean air actions to tackle $PM_{2.5}$ pollution between 2013 and 2020, Nat. Geosci., 17, 987-994, doi: 10.1038/s41561-024-01540-z, 2024.

Lundberg, S.M., Erion, G., Chen, H., DeGrave, A., Prutkin, J.M., Nair, B., Katz, R., Himmelfarb, J., Bansal, N., Lee, S.I.: From local explanations to global understanding with explainable AI for trees. Nat. Mach. Intell., 2, 56-67, doi: 10.1038/s42256-019-0138-9, 2020.

Mallapaty, S.: Chian's extreme weather challenges scientists trying to study it, Nature, 609, 888-888, doi: 10.1038/d41586-022-02954-8, 2022.

Wang, Z.Q., Luo, H.L., Yang, S.: Different mechanisms for the extremely hot central-eastern China in July-August 2022 from a Eurasian large-scale circulation perspective, Environ. Res. Lett., 18, doi: 10.1088/1748-9326/acb3e5, 2023.

Yin, Y., Han, C., Yang, G., Huang, Y., Liu, M., Wang, X.: Changes in the summer extreme precipitation in the Jianghuai plum rain area and their relationship with the intensity anomalies of the south Asian high, Atmos. Res., 236, 104793, doi: 10.1016/j.atmosres.2019.104793, 2020.

Zhang, D.Q., Chen, L.J., Yuan, Y., Zuo, J.Q., Ke, Z.J.: Why was the heat wave in the Yangtze River valley abnormally intensified in late summer 2022? Environ. Res. Lett., 18, doi: 10.1088/1748-9326/acba30, 2023.